A 2 Low Reynolds Number Hydrodynamics – Mesoscale Simulation Techniques

Roland G. Winkler

Institute for Advanced Simulation

Forschungszentrum Jülich GmbH

Contents

Lecture Notes of the Summer School "Microswimmers – From Single Particle Motion to Collective Behaviour", organised by the DFG Priority Programme SPP 1726 (Forschungszentrum Jülich, 2015).

1 Introduction

Cell motility is a major achievement of biological evolution and is essential for a wide spectrum of cellular activities [1]. Swimming of uni- and multi-cellular organisms is essential for their search for food (chemotaxis), the reaction to light (phototaxis), and the orientation in the gravitation field (gravitaxis). Microorganisms, such as spermatozoa, bacteria, protozoa, and algae, use flagella—whip-like structures protruding from their bodies—for their propulsion [1–4]. Furthermore, flagellar motion plays a major role in higher organisms [5,6], where they transport fluid in the respiratory system in form of cilia [7], are involved in cellular communications [8], and even determine the morphological left-right asymmetry in the embryo [9].

Unicellular swimmers, e.g., bacteria like *Escherichia coli*, spermatozoa, and *Paramecia* are typically of a few to several tens of micrometers in size. The physics ruling the swimming on this micrometer scale is very different from that applying to swimming in the macro-world. Swimming at the micrometer scale is swimming at low Reynolds numbers [10], where viscous damping by far dominates over inertia. Hence, swimming concepts of the high Reynolds number macro-world are ineffective on small scales. In the evolutionary process, microorganisms acquired propulsion strategies, which successfully overcome and even exploit viscous drag.

Microswimmers hardly ever swim alone. Sperm cells are released by the millions to compete in the run for the egg [11]. Bacteria grow by dividing and invading their surroundings together. In assemblies of motile microorganisms, cooperativity reaches a new level of complexity as they exhibit highly organized movements with remarkable large-scale patterns such as networks, complex vortices, or swarms [4, 12, 13].

Hydrodynamics and hydrodynamic interactions (HI) are fundamental for swimming on the microscale. This includes the propulsion mechanism itself, the synchronized motion of flagella in flagellar bundles of bacteria such as *E. coli* or *Salmonella*, in cilia beating of cilia arrays, which form metachronal waves [14], and even extends to collective behaviors.

Hydrodynamic interactions pose a major challenge in computer simulation of swimming systems due to the presence of disparate time and length scales as well as far from equilibrium strong spatially and temporally varying forces. As a consequence, coarse-grained or mesoscopic simulation approaches are adopted that mimic the behavior of atomistic systems on the length scales of interest. Established examples of such approaches are Dissipative Particle Dynamics (DPD) [15–17], Lattice Boltzmann (LB) [18–20], Direct Simulation Monte Carlo (DSMC) [21–23], and Multiparticle Collision dynamics (MPC) [24–26]. All the approaches are essentially alternative ways of solving the Navier-Stokes equations for the fluid dynamics. Common to them is a simplified, coarse-grained description of the fluid degrees of freedom while maintaining the essential microscopic physics on the length scales of interest, providing at the same time a computationally efficient implementation in complex geometries and on parallel computers.

In this contribution, several aspects of mesoscale hydrodynamics will be discussed. First of all, the basic equations of hydrodynamics, the Navier-Stokes equations, will be introduced and its long-range character and dynamical long-time tail will be derived. As an application, the synchronization of microrotors by time-dependent hydrodynamic interactions will be considered. Secondly, the MPC approach will be introduced, and results achieved by this simulation approach for the swimming behavior of *E. coli* cells in bulk and near surfaces be discussed.

2 Hydrodynamics

2.1 Linearised Hydrodynamics

Fluid flow on macroscopic scales is typically described by the Navier-Stokes equations

$$\frac{\partial}{\partial t}\varrho + \boldsymbol{\nabla}\cdot(\varrho\boldsymbol{v}) = 0, \tag{1}$$

$$\varrho\left(\frac{\partial}{\partial t}\boldsymbol{v} + (\boldsymbol{v}\cdot\boldsymbol{\nabla})\boldsymbol{v}\right) = \boldsymbol{\nabla}\cdot\boldsymbol{\sigma} + \boldsymbol{f} \tag{2}$$

in terms of a velocity field $\boldsymbol{v}(\boldsymbol{r},t)$, where $\varrho(\boldsymbol{r},t)$ is the fluid mass density, $\boldsymbol{\sigma}(\boldsymbol{r},t)$ the stress tensor, and $\boldsymbol{f}(\boldsymbol{r},t)$ the volume force density [27–29]. Equation (1) expresses the conservation of mass. Equation (2) is an extension of Newton's equation of motion $m\dot{\boldsymbol{v}}(t) = \boldsymbol{F}$, ($m$ mass, $\boldsymbol{F}$ force) to viscous fluids and reflects the conservation of momentum. Strictly speaking there is also an equation for the conservation of energy [27–29], but we will consider isothermal systems in the following and, hence, the two equations characterize the system. The (symmetric) stress tensor of an isotropic system is given macroscopically by [27]

$$\sigma_{\alpha\beta} = -p\delta_{\alpha\beta} + \sum_{\alpha'\beta'}\eta_{\alpha\beta\alpha'\beta'}\frac{\partial v_{\alpha'}}{\partial r_{\beta'}} = -p\delta_{\alpha\beta} + \eta\left(\frac{\partial v_\alpha}{\partial r_\beta} + \frac{\partial v_\beta}{\partial r_\alpha}\right) - \delta_{\alpha\beta}\left(\frac{2}{3}\eta - \eta^{\mathrm{v}}\right)\boldsymbol{\nabla}\cdot\boldsymbol{v}, \tag{3}$$

with

$$\eta_{\alpha\beta\alpha'\beta'} = \eta(\delta_{\alpha\alpha'}\delta_{\beta\beta'} + \delta_{\alpha\beta'}\delta_{\alpha'\beta}) - \left(\frac{2}{3}\eta - \eta^{\mathrm{v}}\right)\delta_{\alpha\beta}\delta_{\alpha'\beta'}, \tag{4}$$

the local pressure $p = p(\boldsymbol{r},t)$, the shear and bulk viscosities η and η^{v}, and α, β, α', $\beta' \in \{x,y,z\}$. Other constitutive equations can be added. We will additionally consider thermal fluctuations of the fluid, which are described by the stress tensor $\boldsymbol{\sigma}^R$, a Gaussian and Markovian stochastic process with the moments

$$\langle\boldsymbol{\sigma}^R\rangle = 0, \tag{5}$$

$$\langle\sigma^R_{\alpha\beta}(\boldsymbol{r},t)\sigma^R_{\alpha'\beta'}(\boldsymbol{r}',t')\rangle = 2k_BT\eta_{\alpha\beta\alpha'\beta'}\delta(\boldsymbol{r}-\boldsymbol{r}')\delta(t-t'). \tag{6}$$

Here, k_B is the Boltzmann constant and T the temperature. The tensor $\boldsymbol{\eta}$ is defined in Eq. (4). Hence, $\boldsymbol{\sigma}^R$ satisfies the fluctuation-dissipation theorem [30]. With the stress tensor (3) and the random force $\boldsymbol{f}^R = \boldsymbol{\nabla}\cdot\boldsymbol{\sigma}^R$, Eq. (2) turns into

$$\varrho\left(\frac{\partial}{\partial t}\boldsymbol{v} + (\boldsymbol{v}\cdot\boldsymbol{\nabla})\boldsymbol{v}\right) = -\boldsymbol{\nabla}p + \eta\Delta\boldsymbol{v} + \left(\frac{\eta}{3} + \eta^{\mathrm{v}}\right)\boldsymbol{\nabla}(\boldsymbol{\nabla}\cdot\boldsymbol{v}) + \boldsymbol{f} + \boldsymbol{f}^R. \tag{7}$$

In order to asses the relevance of the various terms in Eq. (7), in particular the time-dependent and non-linear inertia terms, we scale the velocity field by a typical value v_0, length by L_0, and time by T_0, as usual [31], which yields the equation

$$Re_T\,\frac{\partial\boldsymbol{v}'}{\partial t'} + Re\,(\boldsymbol{v}'\cdot\boldsymbol{\nabla}')\boldsymbol{v}' = -\boldsymbol{\nabla}'p' + \Delta'\boldsymbol{v}' + \left(\frac{1}{3} + \frac{\eta^{\mathrm{v}}}{\eta}\right)\boldsymbol{\nabla}'(\boldsymbol{\nabla}'\cdot\boldsymbol{v}') + \boldsymbol{f}' + \boldsymbol{f}^{R'}, \tag{8}$$

where the primed quantities are dimensionless and of $\mathcal{O}(1)$. Furthermore, we introduced the Reynolds numbers

$$Re = \frac{\rho v_0 L_0}{\eta} = \frac{v_0 L_0}{\nu}, \quad Re_T = \frac{\rho L_0^2}{\eta T_0} = \frac{L_0^2}{\nu T_0}, \tag{9}$$

with the kinematic viscosity $\nu = \eta/\varrho$ [32, 33]. Typically, T_0 is defined as $T_0 = L_0/v_0$ which yields $Re_T = Re$. For a micrometer size sphere of radius R in water with thermal velocity, i.e., $R = L_0 = 10^{-3}\mu m$, $\eta = 10^{-3} Ns/m^2$, $v_0 = \sqrt{3k_BT/\varrho V} = \sqrt{9k_BT/4\varrho\pi L_0^3}$—$V$ is the volume—, the Reynolds number is $Re \approx 2 \times 10^{-3}$. Since the other terms are $\mathcal{O}(1)$, the left hand side of Eq. (8) is typically neglected and the Navier-Stokes equation (7) reduces to the Stokes equation. In addition, often incompressible fluids are considered, i.e., $\varrho = const.$ and $\boldsymbol{\nabla} \cdot \boldsymbol{v} = 0$, hence, Eq. (7) becomes (Stokes equation)

$$\eta \Delta \boldsymbol{v} - \boldsymbol{\nabla} p + \boldsymbol{f} = 0 \tag{10}$$

without thermal fluctuations [27–29,31,34]. The oscillatory Reynolds number Re_T can be written as $Re_T = \tau_\nu/T_0$, with $\tau_\nu = L_0^2/\nu$. Hence, Re_T is the ratio of the viscose time scale τ_ν for shear wave propagation over the distance L_0 and the characteristic system time T_0. In order to establish proper hydrodynamic interactions, $\tau_\nu/T_0 < 1$ and, hence, $Re_T < 1$.

For microswimmers, $Re = 0$ is typically assumed and their dynamics is described by the Stokes equation (10), which leads to peculiarities in their locomotion as expressed by the scallop theorem [10]. The theorem states: If the sequence of shapes displayed by a swimmer is identical to the sequence of shapes traversed in reverse motion—so-called reciprocal motion—the average position of the body cannot change over one period [2, 10, 33, 35]. The main reason is the time independence of the Stokes equation, which naturally cannot lead to an asymmetry in time. Hence, the mechanism for flow generation—the swimming stroke—has to break time-reversal symmetry. This is of particular importance for the synchronization of flagellar beating of bacteria and algae such as *Chlamydomonas* [1] (see also D.6 *Synchronization* by B. M. Friedrich).

The relevance of the unsteady acceleration term with the oscillatory Reynolds number Re_T depends on the time scale of the physical phenomenon of interest. We will keep this term to analyze time correlations in fluids. However, we will only consider linearized hydrodynamics, which means only small deviations from stationary values. With a zero stationary velocity and $\varrho = \rho + \delta\varrho$, we obtain the linearised Landau-Lifshitz Navier-Stokes equations

$$\frac{\partial}{\partial t}\delta\varrho + \rho \boldsymbol{\nabla} \cdot \boldsymbol{v} = 0, \tag{11}$$

$$\rho \frac{\partial}{\partial t}\boldsymbol{v} = -\boldsymbol{\nabla} p + \eta \Delta \boldsymbol{v} + \left(\frac{\eta}{3} + \eta^{\mathrm{v}}\right) \boldsymbol{\nabla}(\boldsymbol{\nabla} \cdot \boldsymbol{v}) + \boldsymbol{f} + \boldsymbol{f}^R. \tag{12}$$

These are two equations for the two unknown quantities p and $\boldsymbol{v}$. Taking the divergence of Eq. (12), we arrive at the equation

$$\Delta p - \frac{1}{c^2}\frac{\partial^2 p}{\partial t^2} = \nabla \cdot \left(\eta \Delta \boldsymbol{v} + \left(\frac{\eta}{3} + \eta^{\mathrm{v}}\right) \nabla(\nabla \cdot \boldsymbol{v}) + \boldsymbol{f}^R\right). \tag{13}$$

The second derivative with respect to time on the left-hand side follows from Eq. (11) together with the ideal gas equation of state; c is the isothermal velocity of sound.

2.2 Solution of the linearised Landau-Lifshitz Navier-Stokes equations

In order to solve the linear equations (12) and (13), we apply the Fourier transformation

$$\boldsymbol{v}(\boldsymbol{r},t) = \frac{1}{2\pi}\sum_{\boldsymbol{k}}\int \hat{\boldsymbol{v}}(\boldsymbol{k},\omega)e^{-i\boldsymbol{k}\cdot\boldsymbol{r}}e^{i\omega t}d\omega, \tag{14}$$

$$\hat{\boldsymbol{v}}(\boldsymbol{k},\omega) = \frac{1}{V}\int \boldsymbol{v}(\boldsymbol{r},t)e^{i\boldsymbol{k}\cdot\boldsymbol{r}}e^{-i\omega t}d^3r dt \tag{15}$$

for the velocity field, with $k_\alpha = 2\pi n_\alpha/L$, $n_\alpha \in \mathbb{Z}$, and $\boldsymbol{k} \neq 0$. We use periodic boundary conditions for the spatial coordinates, since the results will later be compared with simulations. This yields ($\boldsymbol{f} = 0$)

$$\begin{aligned} i\omega\rho\hat{\boldsymbol{v}} &= i\boldsymbol{k}\hat{p} - \eta k^2\hat{\boldsymbol{v}} - \left(\frac{\eta}{3}+\eta^{\mathrm{v}}\right)k^2\mathbf{P}\hat{\boldsymbol{v}} + \hat{\boldsymbol{f}}^R, \\ \left(\frac{\omega^2}{c^2}-k^2\right)\hat{p} &= i\boldsymbol{k}\cdot\left(\eta k^2\hat{\boldsymbol{v}} + \left(\frac{\eta}{3}+\eta^{\mathrm{v}}\right)k^2\mathbf{P}\hat{\boldsymbol{v}} - \hat{\boldsymbol{f}}^R\right), \end{aligned} \tag{16}$$

where $\mathbf{P}$ is a projection operator with the components $P_{\alpha\beta} = k_\alpha k_\beta/k^2$, which projects a vector along the direction of $\boldsymbol{k}$, and $k = |\boldsymbol{k}|$. With the separation $\hat{\boldsymbol{v}} = \hat{\boldsymbol{v}}^L + \hat{\boldsymbol{v}}^T$ into a longitudinal $\hat{\boldsymbol{v}}^L$ and transverse part $\hat{\boldsymbol{v}}^T$ with respect to $\boldsymbol{k}$, i.e., $\hat{\boldsymbol{v}}\cdot\boldsymbol{k} = \hat{v}^L k$ and $\hat{\boldsymbol{v}}^T\cdot\boldsymbol{k} = 0$, Eqs. (16) yield

$$\hat{\boldsymbol{v}}(\boldsymbol{k},\omega) = \hat{\mathbf{Q}}\hat{\boldsymbol{f}}^R = \left(\hat{\mathbf{Q}}^L + \hat{\mathbf{Q}}^T\right)\hat{\boldsymbol{f}}^R, \tag{17}$$

with

$$\hat{\mathbf{Q}}^L = \left(\tilde{\eta}k^2 + \frac{i\rho}{\omega}[\omega^2 - c^2k^2]\right)^{-1}\mathbf{P} = \hat{Q}^L\mathbf{P}, \tag{18}$$

$$\hat{\mathbf{Q}}^T = \left(\eta k^2 + i\rho\omega\right)^{-1}(\mathbf{E}-\mathbf{P}) = \hat{Q}^T(\mathbf{E}-\mathbf{P}), \tag{19}$$

and $\tilde{\eta} = 4\eta/3 + \eta^{\mathrm{v}}$; $\mathbf{E}$ is the unit matrix [36].
Fourier transformation with respect to time yields ($\Theta(t)$: Heaviside's function)

$$Q^T(\boldsymbol{k},t) = \frac{1}{\rho}e^{-\nu k^2 t}\Theta(t), \tag{20}$$

$$Q^L(\boldsymbol{k},t) = \frac{1}{\rho}e^{-k^2\tilde{\nu}t/2}\left[\cos(\Omega t) - \sqrt{\frac{k^2\tilde{\nu}^2}{4c^2-k^2\tilde{\nu}^2}}\sin(\Omega t)\right]\Theta(t) \tag{21}$$

for $4c^2/(k^2\tilde{\nu}^2) > 1$ and with the abbreviation $\Omega = k^2\tilde{\nu}\sqrt{4c^2/(k^2\tilde{\nu}^2)-1}/2$. The expression for $4c^2/(k^2\tilde{\nu}^2) < 1$ follows by analytical continuation [36].

2.3 Velocity correlation function in Fourier space

With the help of the correlation function for the random force

$$\begin{aligned} \left\langle \hat{f}^R_\alpha(\boldsymbol{k},\omega)\hat{f}^R_\beta(\boldsymbol{k}',\omega')\right\rangle &= -\sum_{\alpha',\beta'}k_{\alpha'}k'_{\beta'}\left\langle\hat{\sigma}^R_{\alpha\alpha'}(\boldsymbol{k},\omega)\hat{\sigma}^R_{\beta\beta'}(\boldsymbol{k}',\omega')\right\rangle \\ &= \frac{4\pi k_B T}{V}\boldsymbol{k}^2\left[\eta\delta_{\alpha\beta} + \left(\frac{1}{3}\eta+\eta^{\mathrm{v}}\right)\frac{k_\alpha k_\beta}{k^2}\right]\delta(\omega+\omega')\delta_{\boldsymbol{k},-\boldsymbol{k}'}, \end{aligned} \tag{22}$$

velocity autocorrelation functions in Fourier space can easily be calculate [36]; in particular,

$$\langle \hat{\boldsymbol{v}}(\boldsymbol{k},\omega)\cdot\hat{\boldsymbol{v}}(\boldsymbol{k}',\omega')\rangle = \frac{4\pi k_B T}{V}k^2\left(2\eta|\hat{Q}^T|^2+\tilde{\eta}|\hat{Q}^L|^2\right)\delta(\omega+\omega')\delta_{\boldsymbol{k},-\boldsymbol{k}'} \tag{23}$$

is obtained by Eqs. (17), (18), and (19). The factor 2 in front of $|Q^T|^2$ reflects the two transverse components of vorticity
The time-dependent correlation function $\langle \boldsymbol{v}(\boldsymbol{k},t)\cdot\boldsymbol{v}(\boldsymbol{k}',0)\rangle$ follows by convolution

$$\langle \boldsymbol{v}(\boldsymbol{k},t)\cdot\boldsymbol{v}(\boldsymbol{k}',0)\rangle = \frac{2k_BTk^2}{V}\delta_{\boldsymbol{k},-\boldsymbol{k}'}\int\left[2\eta Q^T(\boldsymbol{k},t-t')Q^T(\boldsymbol{k}',-t')+\tilde{\eta}Q^L(\boldsymbol{k},t-t')Q^L(\boldsymbol{k}',-t')\right]dt'. \tag{24}$$

Explicitly, we find for the
(i) transverse velocity autocorrelation function

$$\left\langle \boldsymbol{v}^T(\boldsymbol{k},t)\cdot\boldsymbol{v}^T(-\boldsymbol{k},0)\right\rangle = \frac{2k_BT}{\rho V}e^{-\nu k^2|t|}, \tag{25}$$

(ii) longitudinal velocity autocorrelation function

$$\left\langle v^L(\boldsymbol{k},t)v^L(-\boldsymbol{k},0)\right\rangle = \frac{k_BT}{\rho V}e^{-\tilde{\nu}k^2|t|/2}\left[\cos(\Omega|t|)-\sqrt{\frac{k^2\tilde{\nu}^2}{4c^2-k^2\tilde{\nu}^2}}\sin(\Omega|t|)\right]. \tag{26}$$

The transverse correlation function decays simply in an exponential manner, with a characteristic time $\tau_\nu = 1/\nu k^2$ determined by the kinematic viscosity and the wave vector. The longitudinal correlation function decays with a different factor (sound attenuation coefficient) involving $\tilde{\nu}/2$ and exhibits oscillations with the frequency Ω. Examples are provided in Fig. 5.

2.4 Velocity correlation function in real space—long-time tail

Adopting the Lagrangian description of the fluid, where a fluid element is followed as it moves through space and time, we additionally average the correlation function over the distribution of displacements $\boldsymbol{r}-\boldsymbol{r}'$. Hence, Fourier transformation of Eq. (24) with respect to $\boldsymbol{k}$ leads to

$$\langle \boldsymbol{v}(t)\cdot\boldsymbol{v}(0)\rangle = \sum_{\boldsymbol{k}}\langle \boldsymbol{v}(\boldsymbol{k},t)\cdot\boldsymbol{v}(-\boldsymbol{k},0)\rangle\left\langle e^{-i\boldsymbol{k}\cdot(\boldsymbol{r}-\boldsymbol{r}')}\right\rangle. \tag{27}$$

Assuming a diffusive motion of the fluid element, with Gaussian distributed displacements, we find

$$\begin{aligned}\langle \boldsymbol{v}(t)\cdot\boldsymbol{v}(0)\rangle &= \sum_{\boldsymbol{k}}\langle \boldsymbol{v}(\boldsymbol{k},t)\cdot\boldsymbol{v}(-\boldsymbol{k},0)\rangle\exp\left(-k^2\left\langle(\boldsymbol{r}(t)-\boldsymbol{r}(0))^2\right\rangle/6\right)\\ &= \frac{k_BT}{V}\sum_{\boldsymbol{k}}\left[2Q^T(\boldsymbol{k},t)+Q^L(\boldsymbol{k},t)\right]e^{-k^2Dt}.\end{aligned} \tag{28}$$

Here, $\langle(\boldsymbol{r}(t)-\boldsymbol{r}(0))^2\rangle$ is the mean square displacement, which, in the simplest case, reduces to $\langle(\boldsymbol{r}(t)-\boldsymbol{r}(0))^2\rangle = 6Dt$, with D the diffusion coefficient.

In general, the sum over $\boldsymbol{k}$ in Eq. (28) cannot be evaluated analytically. For the transverse velocity correlation function, however, we obtain the expression

$$\left\langle \boldsymbol{v}^T(t) \cdot \boldsymbol{v}^T(0) \right\rangle = \frac{2k_BT}{\rho(2\pi)^3} \int e^{-\nu k^2 t} e^{-Dk^2 t} d^3k = \frac{k_BT}{4\rho} \frac{1}{[\pi(\nu + D)t]^{3/2}}. \tag{29}$$

in the limit of an infinitely large system ($L \to \infty$, $\sum_{\boldsymbol{k}} \to V/(2\pi)^3 \int d^3k$). Hence, we find the well-known long-time tail of the transverse velocity correlation function—a major characteristics of hydrodynamics [36–45].

2.5 Hydrodynamic tensor in real space—Oseen tensor

We will now consider the mean velocity field $\boldsymbol{u}(\boldsymbol{r}, t) = \langle \boldsymbol{v}(\boldsymbol{r}, t) \rangle$, where the thermal fluctuations $\boldsymbol{f}^R$ have been averaged out. Focusing on the transverse part of the hydrodynamic tensor only, e.g., for an incompressible fluid, the flow field can be expressed as

$$\boldsymbol{u}(\boldsymbol{r}, t) = \sum_{\boldsymbol{k}} e^{-i\boldsymbol{k}\cdot\boldsymbol{r}} \int_0^t \mathbf{Q}^T(\boldsymbol{k}, t - t') \boldsymbol{f}(t')\, dt' \tag{30}$$

starting from Eq. (17). We will assume that the force $\boldsymbol{f}$ changes much more slowly with time than the tensor $\mathbf{Q}^T$. Then, $\boldsymbol{f}$ can be taken out of the integral and the upper integration limit can be extended to infinity. Hence,

$$\boldsymbol{u}(\boldsymbol{r}, t) = \sum_{\boldsymbol{k}} e^{-i\boldsymbol{k}\cdot\boldsymbol{r}} \frac{1}{\eta k^2} \left(\mathbf{E} - \mathbf{P}\right) \boldsymbol{f}(t) = \sum_{\boldsymbol{k}} e^{-i\boldsymbol{k}\cdot\boldsymbol{r}} \mathbf{Q}^T(\boldsymbol{k}) \boldsymbol{f}(t). \tag{31}$$

For an infinite system, Fourier transformation yields $\boldsymbol{u}(\boldsymbol{r}, t) = \mathbf{Q}^T(\boldsymbol{r})\boldsymbol{F}$, where $\boldsymbol{F} = V\boldsymbol{f}$ and

$$\mathbf{Q}^T(\boldsymbol{k}) = \frac{1}{\eta k^2} \left(\mathbf{E} - \mathbf{P}\right) , \tag{32}$$

$$\mathbf{Q}^T(\boldsymbol{r}) = \frac{1}{8\pi\eta|\boldsymbol{r}|} \left(\mathbf{E} + \frac{\boldsymbol{r}\boldsymbol{r}^T}{|\boldsymbol{r}|^2}\right) \tag{33}$$

are the well-known Oseen tensors in Fourier and real space, respectively [31, 34]. Here, $\boldsymbol{r}^T$ is the transpose of the vector $\boldsymbol{r}$. The Oseen tensor reflects another important property of hydrodynamic interactions, namely their long-range character, i.e., $Q(r) \sim 1/r$. Note that the same tensor follows directly as solution of the Stokes equation (10) for an incompressible fluid.

The various hydrodynamic properties have to been accounted for by hydrodynamic simulation algorithms.

2.6 Hydrodynamic synchronization of microrotors

Synchronization of motion is a common phenomenon in nonlinear many-particle systems, and thus appears in a broad range of physical, biological, engineering, and social systems [33, 46, 47]. Various aspects of synchronization will be discussed in the lecture D.6 *Synchronization* by B. M. Friedrich. Here, I want to illustrate time-dependent hydrodynamic effects on synchronization of rotors.

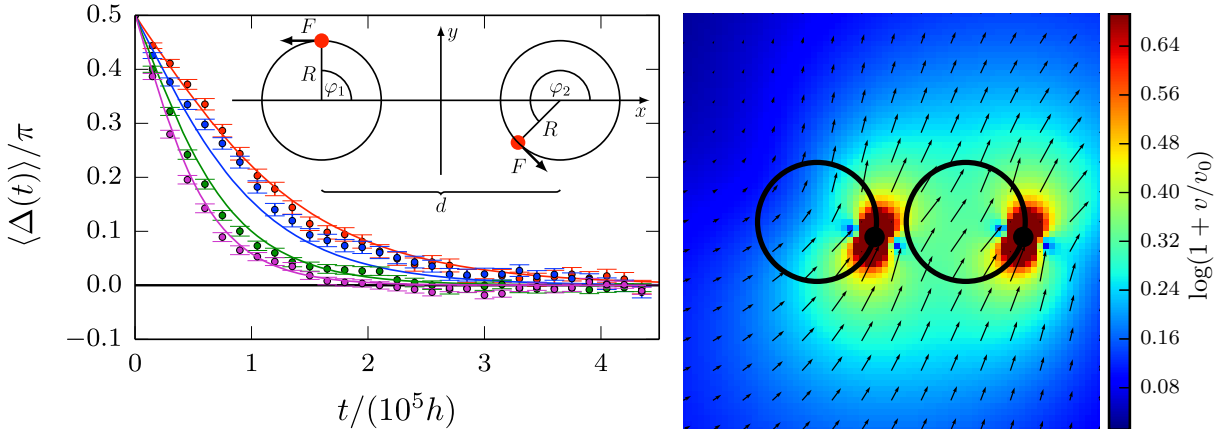

Fig. 1: *(Left) Average phase-angle difference* $\Delta(t)$ *for the Péclet numbers* $Pe = 120,\ 140,\ 160,$ *and* 180 *(top to bottom). Symbols represent simulation results and the solid lines are obtained by numerical integration of Eq. (36) including transversal and longitudinal modes of the hydrodynamic tensor. Inset: Model system of hydrodynamically coupled rotors. The beads move along fixed circular trajectories in the* xy*-plane, each driven by a constant tangential force* F*. (Right) Flow field in the stationary synchronized state for the Péclet number* $Pe = 120$*. The reddish colors indicate the dipolar character of the flow field. The flow field is calculated via Eq. (37). For details see Refs. [33, 45].*

From a microswimmer point of view, a rotor is the most simple description of a beating cilium [48]. For example, its endpoint moves along a closed trajectory, which might be approximated by a circle. The rotor model is illustrated in the inset of Fig. 1. The two beads of radius R_H move along circles of radius R, each driven by an active force $\boldsymbol{F}_i$. The circles are centered at $\boldsymbol{r}_i^0 = (-1)^i(d/2)\hat{\boldsymbol{e}}_x$ $(i = 1, 2)$, where $\hat{\boldsymbol{e}}_x$ is the unit vector along the x-axis and d the center-to-center distance. The trajectories of the bead centers can be expressed as

$$\boldsymbol{r}_i(t) = \boldsymbol{r}_i^0 + R(\cos\varphi_i(t), \sin\varphi_i(t), 0)^T, \tag{34}$$

in terms of the phase angles $\varphi_i(t)$. The driving forces $\boldsymbol{F}_i(t) = F\hat{\boldsymbol{t}}_i(t)$ are of equal magnitude and point along the tangents $\hat{\boldsymbol{t}}_i(t) = (-\sin\varphi_i(t), \cos\varphi_i(t), 0)^T$.
The equations of motion of the points are given by

$$\dot{\boldsymbol{r}}_i(t) = \frac{1}{\gamma}\boldsymbol{F}_i(t) + \sum_{j\neq i}\int_0^t \mathbf{Q}(\boldsymbol{r}_i(t) - \boldsymbol{r}_j(t'), t - t')\ \boldsymbol{F}_j(t')\ dt' \tag{35}$$

in terms of the hydrodynamic tensor of Eq. (17) with the components of Eqs. (20) and (21). Here, thermal fluctuations are only included via the hydrodynamic tensor. For a numerical treatment, the simpler, approximate expressions for the dynamics of the phase angles

$$\dot{\varphi}_i = \omega + \frac{F}{R}\sum_{j\neq i}\int_0^t \hat{\boldsymbol{t}}_i(t)\cdot\mathbf{Q}(d\boldsymbol{e}_x, t - t')\ \hat{\boldsymbol{t}}_j(t')\ dt', \tag{36}$$

derived within the mean-field approximation $\boldsymbol{R}_2(t) - \boldsymbol{R}_1(t') \approx \boldsymbol{d} = d\hat{\boldsymbol{e}}_x$, are sufficient, where $\omega = F/\gamma R$ is the intrinsic angular frequency and $\gamma = 6\pi\eta R_H$ Stokes' friction coefficient of a bead [33, 45].

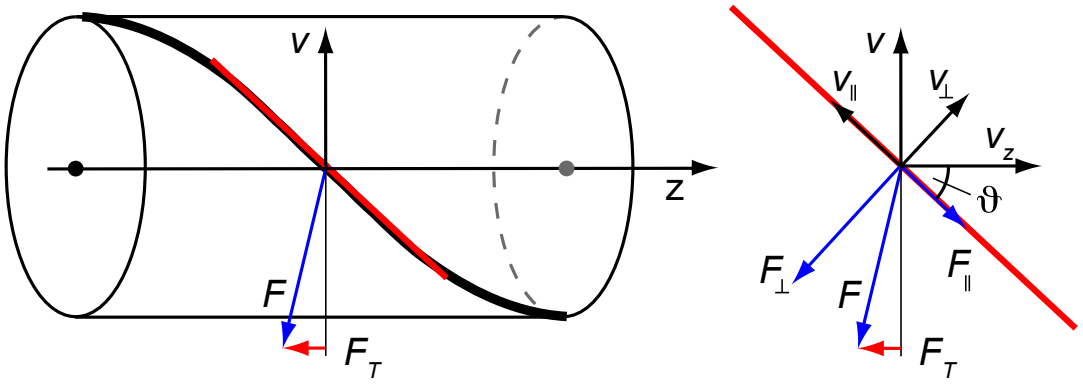

Fig. 2: *Helical segment moving in a viscous fluid. Only half of a helical pitch is shown. The drag-based thrust force $\boldsymbol{F}_T$ appears by the motion of the red rodlike segment in the direction $\boldsymbol{v}$. For details see Refs. [1, 3].*

Figure 1 shows phase-angle differences $\Delta(t) = \varphi_1(t) - \varphi_2(t)$ of co-rotating beads calculated according to Eq. (36) and obtained from MPC simulations (see Sec. 3.1). Interestingly, the beads exhibit synchronization of their rotational motion despite strong thermal fluctuations for the various Péclet numbers Pe, where Pe is defined as $Pe = FR/k_BT$ [33]. The simulation results compare well with the theoretical predictions of Eqs. (36), although there are small differences for $Pe = 140$ and 160.

The flow field

$$\boldsymbol{v}(\boldsymbol{r},t) = F\sum_{i=1}^{2}\int_0^t \mathbf{Q}(\boldsymbol{r}-\boldsymbol{r}_i(t'),t-t')\hat{\boldsymbol{t}}_i(t')\,dt' \tag{37}$$

is illustrated in Fig. 1 (right). The velocity profile decays very fast with separation from a beat. Thereby, it is anisotropic—-of Stokeslet shape—with a slower decay in the tangential forward and backward direction. The synchronous state is preferable, because it minimizes dissipation.

Naturally, synchronization by time-dependent hydrodynamic interactions is possible, because the time reversibility of the underlying dynamical equations is broken, despite a time-reversible cyclic rotor motion. We find the dependence $t_s/T_r \sim 1/\sqrt{Re_T}$ of the synchronization time on the oscillatory Reynolds number, where T_r is the rotational period of a rotor [33]. Hence, t_s approaches infinity for $Re_T \to 0$, i.e., for systems where the period is far larger than the viscous time. However, the transition is gradual, which implies a continuous breakdown of synchronization. Only for $Re_T = 0$, there is no synchronization anymore, in analogy with the scallop theorem [33, 35]

2.7 Propulsion of rotating helix

As mentioned in the introduction, propulsion of a rotating helical filament in a viscous fluid appears due to hydrodynamic interactions. To illustrated the appearing thrust force $\boldsymbol{F}_T$, the geometry of Fig. 2 is considered. The helix moves in the direction $\boldsymbol{v}$ by rotation. To calculate the (local) friction force, the helical segment is approximated by a rod (red). Separation of the

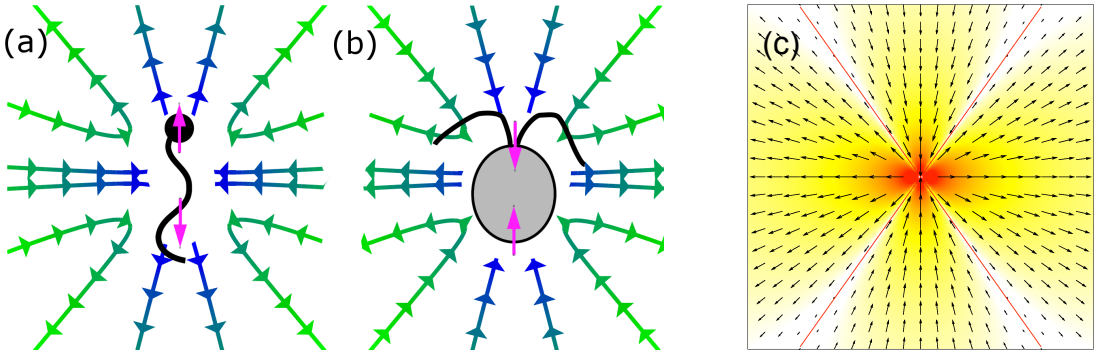

Fig. 3: *Schematics of the flow field of dipole swimmers; (a) pusher and (b) puller. (c) Flow lines of a hydrodynamic dipole aligned horizontally according to Eq. (39). For details see Ref. [1].*

velocity $\boldsymbol{v}$ it its components parallel ($\boldsymbol{v}_\parallel$) and perpendicular ($\boldsymbol{v}_\perp$) to the rod yields the respective friction forces $\boldsymbol{F}_\parallel = -\gamma_\parallel \boldsymbol{v}_\parallel$ and $\boldsymbol{F}_\perp = -\gamma_\perp \boldsymbol{v}_\perp$. Here, the distinct friction coefficients parallel ($\gamma_\parallel$) and perpendicular ($\gamma_\perp$) to the rod orientation are used. In the asymptotic limit of an infinitely long rod, the ratio between the coefficients is $\gamma_\parallel/\gamma_\perp = 1/2$. Explicit expression for the two values can be obtained by the Oseen tensor (33) [1, 34, 49]. The thrust force is given by $F_T = -\gamma_\parallel v_{\parallel,z} - \gamma_\perp v_{\perp,z}$. Simple geometrical considerations yield then

$$F_T = (\gamma_\parallel - \gamma_\perp) v \sin\vartheta \cos\vartheta. \tag{38}$$

Hence, propulsion only appears due to frictional anisotropy of the helix. More precise calculations and expressions for the friction coefficients are presented in Refs. [1, 50, 51].

2.8 Dipole swimmer

Biological swimmers move autonomously, free from any net external force or torque. Hence, the total interaction force of the swimmer on the fluid, and vice versa, vanishes. In the simplest case, which actually applies to many microswimmers like bacteria, spermatozoa, or algae, the far-field hydrodynamics (at distances much larger than the swimmer size) can then well be described by a force dipole [1–3,52]. This has been confirmed experimentally and by simulation for *E. coli* in Refs. [53, 54] (see also Sec. 4.1). Two classes of such dipole swimmers can be distinguished, as shown schematically in Fig. 3. If the swimmer has its motor in the back, and the passive body drags along the surrounding fluid in front, the characteristic flow field of a pusher emerges, e.g., *E. coli*. Similarly, if the swimmer has its motor in the front, and the passive body drags along the surrounding fluid behind, the characteristic flow field of a puller develops. It is important to notice that the flow fields of pushers and pullers look similar, but with opposite flow direction, which has important consequences for the interactions between swimmers and of swimmers with walls.

Mathematically, the flow field $\boldsymbol{u}_d(\boldsymbol{r} - \boldsymbol{r}_0)$ of a hydrodynamic force dipole located at r_0 can be obtained easily from the Oseen tensor of Eq. (33) by considering two opposite forces $\boldsymbol{f} = f\hat{\boldsymbol{e}}$ of equal magnitude acting on the fluid at $\boldsymbol{r} = \boldsymbol{r}_0 \pm \boldsymbol{d}/2$, with $\boldsymbol{d} = d\hat{\boldsymbol{e}}$. An expansion to leading order in $\boldsymbol{d}/|\boldsymbol{r} - \boldsymbol{r}_0|$ yields

$$\boldsymbol{u}_d(\boldsymbol{r}) = \frac{P}{8\pi\eta r^3}\left[-1 + 3\frac{(\boldsymbol{r}\cdot\hat{\boldsymbol{e}})^2}{r^2}\right]\boldsymbol{r}, \tag{39}$$

where $P = fd$ is the dipole strength. Note that the flow field of a force dipole decays as $1/r^2$ from the center of the dipole, faster than the force monopole or Stokeslet of Eq. (33). The flow lines of a hydrodynamic dipole oriented vertically are shown in Fig. 3(c). There are two inflow and two outflow regions in the xy-projection, which are separated by the separatrices $y = \sqrt{2}x$. In three dimensions, the out-flow region is a cone.
In general, higher order multipoles can be derived and be used to describe the flow field of (complex) microswimmers [2].

3 Mesoscale hydrodynamic simulations

The macroscopic flow behavior is rather similar for many fluids even though the microscopic structure is quite different. The microscopic details may influence the absolute values of transport coefficients, however, the form of the macroscopic hydrodynamic equations is solely determined by symmetries and conservation laws. This is the basis for various mesoscale hydrodynamic simulations approaches, which select particular "microscopic" dynamical equations, but yield hydrodynamics on large scales and long times.

3.1 Multiparticle Collision Dynamics

In MPC, the fluid is represented by N point particles of mass m. The algorithm consists of individual streaming and collision steps (cf. Fig. 4). In the streaming step, the particles move independent of each other and experience only possibly present external forces. Without such forces, they move ballistically and their positions $\boldsymbol{r}_i$ are updated according to

$$\boldsymbol{r}_i(t+h) = \boldsymbol{r}_i(t) + h\boldsymbol{v}_i(t), \tag{40}$$

where $\boldsymbol{v}_i$ is the velocity of particle i and h is the time interval between collisions, which will be denoted as collision time. In the collision step, a coarse-grained interaction between the fluid particles is imposed by a stochastic process. For this purpose, the system is divided in cubic cells of side length a to define the collisional environment. An elementary requirement is that the stochastic process conserves momentum on the collision-cell level, only then hydrodynamics emerges on large length scales. There are various possibilities for such a process, namely the stochastic rotation dynamics (SRD) approach [24] and the assignment of new Gaussian distributed random relative velocities ("Andersen thermostat" (AT)) [55–57]. Here, I will focus on the MPC-SRD implementation.
In MPC-SRD, the relative velocities $\boldsymbol{v}_i - \boldsymbol{v}_{cm}$, with respect to the center-of-mass velocity $\boldsymbol{v}_{cm}$ of a cell, are rotated around an axis by a fixed angle α [24–26, 58], i.e,

$$\boldsymbol{v}_i(t+h) = \boldsymbol{v}_i(t) + (\mathbf{R}(\alpha) - \mathbf{E})\left(\boldsymbol{v}_i(t) - (t)\right), \tag{41}$$

where $\mathbf{R}$ is the rotation matrix [59], and

$$\boldsymbol{v}_{cm} = \frac{1}{N_c}\sum_{i=1}^{N_c} \boldsymbol{v}_i \tag{42}$$

of the N_c particles contained in the cell of particle i. The orientation of the rotation axis is chosen randomly for every collision cell and time step. As is easily shown, the algorithm conserves

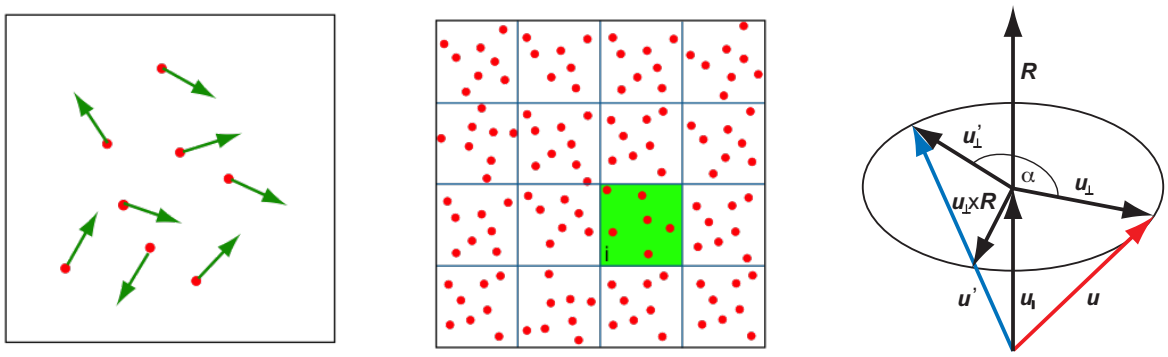

Fig. 4: *Illustration of the MPC-SRD dynamics: (left) streaming of particles; (middle) sorting of particles in collision cells. (Right) Rotation of the vector* $\boldsymbol{u}$ *to* $\boldsymbol{u}'$ *around the axis along* $\boldsymbol{R}$ *by the angle* α*.* $\boldsymbol{u}_\parallel$ *and* $\boldsymbol{u}_\perp$ *denote the vectors parallel and perpendicular to* $\boldsymbol{R}$*, respectively [55, 59].*

mass, momentum, and energy in every collision cell. The velocity distribution is given by the Maxwell-Boltzmann distribution in the limit $N \to \infty$ [59, 60].

This MPC algorithm violates angular momentum conservation. In Refs. [33, 56, 57] algorithms are presented, which additionally preserve angular momentum. More importantly, partition of space into collision cells implies a violation of Galilean invariance. In Refs. [61, 62], a random shift of the entire collisional grid is introduced to restore Galilean invariance. In practice, for sorting into collision cells, all particles are shifted by the same random vector with Cartesian components uniformly distributed in the interval $[-a/2, a/2]$. As a consequence, no reference frame is preferred. A canonical ensemble is obtained under isothermal conditions. This is achieved by a velocity scaling procedure as described in Refs. [59, 60]. In addition, a virial-based stress tensor of the fluid has been presented in Ref. [63]. Moreover, analytical expressions have be derived for the transport coefficients, i.e., the diffusion coefficient of a fluid particle and the fluid viscosity [63–65].

3.2 Hydrodynamics and Multiparticle Collision Dynamics

In order to characterize the hydrodynamic properties of the MPC fluid, we considered three-dimensional systems and applied periodic boundary conditions.

Figure 5 provides examples of hydrodynamic correlations of a MPC fluid. The expected exponential decay of Eq. (25) is clearly present (left), as well as the long-time tail Eq. (29) (middle). The oscillations for long times are due to sound propagation in the periodic system. Figure 5 (right) shows the k dependence of the MPC fluid hydrodynamic tensor, which follows by integration of the fluid correlation function in the limit $t \to \infty$. We evidently obtain the dependence $Q^T = 1/\eta k^2$ for sufficiently small k values, i.e, sufficiently large lengths scales. More details are presented in Ref. [36].

These results clearly show that MPC is a suitable simulation approach for fluids, since it captures their essential aspects. Naturally, a quantitative agreement with the solution of the Navier-Stokes equations can only be expected on sufficiently large length and times scales. In terms of length scale, this means scales larger than the collision cell size or, if the mean free path of a MPC particle is larger than a, larger than its mean-free path. As far as time is concerned, shear and sound waves should have propagated over one collision cell, i.e., $t > \tau_\nu \approx a^2/\nu$. This is

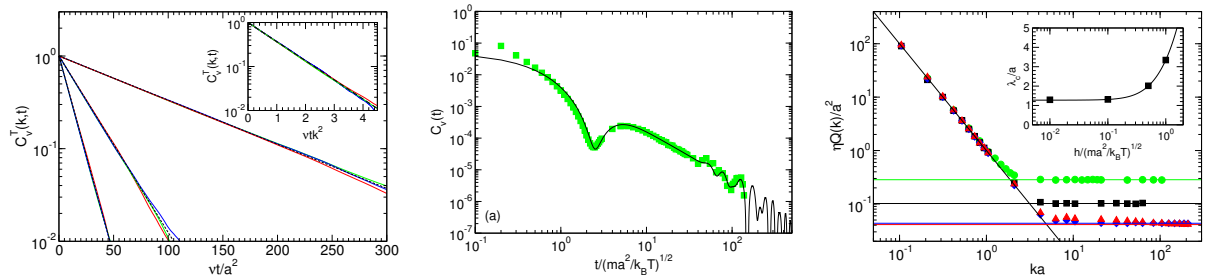

Fig. 5: *Example of MPC-fluid correlations. (left) Normalized transverse velocity autocorrelation in Fourier space. Inset: universal dependence on $\nu k^2 t$. (middle) Magnitude of the normalized velocity autocorrelation function (27). The oscillations at longer times are due to sound propagation in the periodic system. (right) Dependence of the hydrodynamics tensor $Q(k)$ (33) on the wave number for various fluid viscosities; $Q(k) \sim 1/k^2$ for $ka \lesssim 2$. Note that longitudinal (sound) modes do not contribute to the long-time behavior. For details see Ref. [36].*

consistent with the simulation results.

3.3 MPC: Embedded object and boundary conditions

A very simple procedure for coupling embedded objects such as colloids or polymers to a MPC fluid has been proposed in Refs. [66–69]. In this approach, a colloidal particle or a polymer is composed of point particles which are connected by a suitable bond potential to maintain the respective shape. To couple the object to the MPC fluid, the individual particles (monomers) participate in the MPC collision. If particle (monomer) k has mass M and velocity $\boldsymbol{V}_k$ the center-of-mass velocity of all particles (MPC and monomers) in a collision cell is

$$\boldsymbol{v}_{cm} = \frac{\sum_{i=1}^{N_c} m\boldsymbol{v}_i + \sum_{k=1}^{N_m^c} M\boldsymbol{V}_k}{mN_c + MN_m^c}, \tag{43}$$

where N_m^c is the number of monomers in the collision cell. A stochastic rotation of the relative velocities of both the fluid particles and embedded monomers is then performed in the collision step, which leads to an exchange of momentum between them. The dynamics of the monomers is typically treated by molecular dynamics simulations (MD), applying the velocity Verlet integration scheme [70, 71]. Hence, the new monomer momenta are used as initial conditions for the subsequent streaming step (MD) of duration h involving several MD steps, since the MD simulation time step is typically smaller than h. In this approach, the average mass of fluid particles per cell $m\langle N_c\rangle$ should be of the order of the total monomer mass MN_m^c. This corresponds to a neutrally buoyant object which responds quickly to the fluid flow but is not kicked around too violently. It is also important to note that the average number of monomers per cell $\langle N_m\rangle$ should be on the order of unity to properly resolve HI between them. On the other hand, the average bond length in a semiflexible polymer or rodlike colloid should not be much larger than the cell size a, in order to capture the anisotropic friction of rodlike molecules due to HI (which leads to a twice as large perpendicular than parallel friction coefficient for long stiff rods [31, 34]), and to avoid an unnecessarily large ratio of the number of fluid-to-solute particles. Hence, the average bond length should be of order a.

To accurately resolve the local flow field around a hard-sphere colloid, methods have been proposed which exclude fluid-particles from the interior of the colloid and mimic slip [58, 72] or no-slip boundary conditions [26, 73–77]. No-slip boundary conditions are modeled by the bounce-back rule. Here, the relative velocity of a fluid particle $\tilde{\boldsymbol{v}}_i = \boldsymbol{v}_i - \boldsymbol{v}_s$, where $\boldsymbol{v}_s$ is the velocity of the surface point $\boldsymbol{r}_s$ hit by the particle i, is inverted from $\tilde{\boldsymbol{v}}_i$ to $-\tilde{\boldsymbol{v}}_i$, when it intersects the surface of an impenetrable particle, e.g., a colloid, a blood cell, or a wall. The velocity $\boldsymbol{v}_s$ may comprise translational and rotational components, i.e, $\boldsymbol{v}_s(\boldsymbol{r}_s) = \boldsymbol{V} + \boldsymbol{\omega} \times (\boldsymbol{r}_s - \boldsymbol{R})$, where $\boldsymbol{V}$ and $\boldsymbol{R}$ are the center-of-mass velocity and position of the colloid, respectively, and $\boldsymbol{\omega}$ is its rotational frequency.
Since walls or surfaces will generally not coincide with the collision cell boundaries, in particular due to a random shift, the simple bounce-back rule fails to guarantee no-slip boundary conditions. To establish no-slip boundary conditions or at least reduce slip as far as possible, the following procedure has been suggested [73]: For all collision cells that are intersected by walls, fill the wall part of the cell with a sufficient number of virtual (phantom) particles in order to ensure that the total number of particles is equal to $\langle N_c \rangle$. The velocities of the wall particles are taken from a Maxwell-Boltzmann distribution with an appropriate mean and variance $k_B T/m$ (for details see Refs. [75–77]). Since the sum of Gaussian random numbers is also Gaussian distributed, the velocities of the individual virtual particles need not be determined explicitly in simple geometries, it suffices to determine a momentum $\boldsymbol{p}$ from a Maxwell-Boltzmann distribution with zero mean and variance $mN_p k_B T$, where $N_p = \langle N_c \rangle - N_{sc}$ is the number of virtual particles corresponding to the partially filled cell of N_{sc} particles. The center-of-mass velocity of the cell is then

$$\boldsymbol{v}_{cm} = \frac{1}{m \langle N_c \rangle} \left(\sum_{i=1}^{N_{sc}} m\boldsymbol{v}_i + \boldsymbol{p} \right). \tag{44}$$

Results for a Poiseuille flow obtained by this procedure are in good agreement with the correct parabolic flow profile [60, 73]. A more advanced method, taking into account fluctuations of virtual particles in a collision cell is described in Refs. [59, 63].

4 Swimming of bacteria

As an examples of the MPC approach and the relevance of hydrodynamics, the swimming behavior of a model of an *E. Coli* bacterium will be discussed.

4.1 Flow field of *E. coli* in bulk

The bacterium consists of a body and flagellar filaments, as shown in Fig. 6, which are composed of point particles of mass $M = 10m$. The cell body is represented by a spherocylinder of diameter $d = 9a$ and length $\ell_\mathrm{b} = 25a$. In each of the 49 sections, 60 particles are uniformly distributed along circles on the spherocylinder surface. To maintain the shape of the body, various particles, specifically nearest- and next-nearest-neighbors, are bonded by a harmonic potential of finite length. A flagellum is described by the helical wormlike-chain model, [78, 79] with an adaptation suitable for the combination with MPC. As shown in Fig. 6(b), a flagellum consists of $N = 76$ segments with a total of 381 particles. In each segment, six particles are arranged in an octahedron of edge length $a/\sqrt{2}$, forming 12 bonds along the edges and three along the diagonals. The preferred bond lengths are $r_\mathrm{e} = a/\sqrt{2}$ for edges and $r_\mathrm{e} = a$ for diagonals.

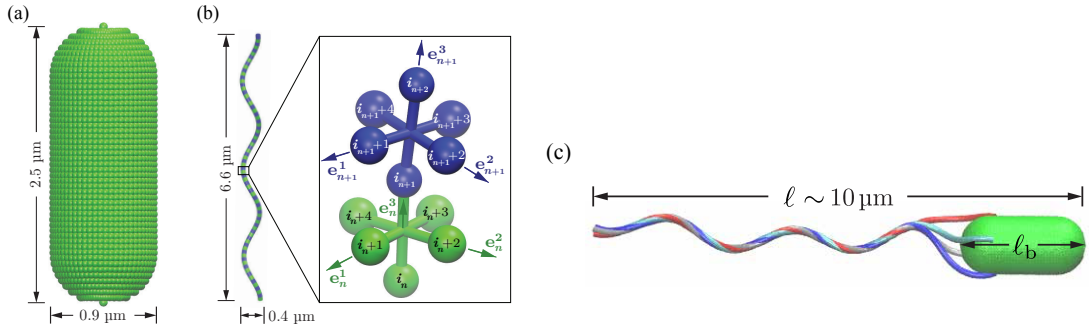

Fig. 6: *(a) Model of the spherocylindrical cell body of diameter $d = 9a = 0.9$ µm and length $\ell_\mathrm{b} = 25a = 2.5$ µm. It is composed of 51 circular sections of particles, which are connected by harmonic bonds of finite length. (b) The flagellum, a three-turn left-handed helix of radius $R = 0.2$ µm, pitch $\Lambda = 2.2$ µm, and contour length $L_c = 7.6$ µm (corresponding to the parallel length $L_\parallel = 6.6$ µm), consists of 76 consecutive segments. (c) Swimming model bacterium. For details see Ref. [54].*

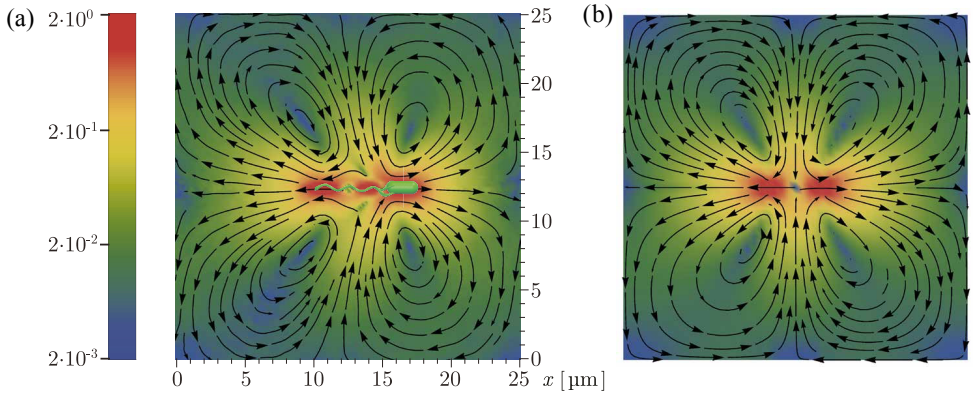

Fig. 7: *(a) Time-averaged flow field generated by a single swimming bacterium in a simulation box with periodic boundary conditions. (b) Flow profile for a finite-distance force dipole for the same geometry. For details see Ref. [54].*

The octahedron construction allows for a straightforward description of the intrinsic twist of the flagellum and a coupling of the twist to the forces exerted by the MPC fluid.

The flow field created by the rotating cell body and counter-rotating flagellar bundle is displayed in Fig. 7(a). The flow pattern not too close to the bacterium approximately resembles that of swimming *E. coli* determined from experiments (see Fig. 1A in Ref. [53]). Closer to the bacterium, the flow field exhibits specific features reflecting the bacterium's detailed structure. In particular, the flow field reveals a front-back asymmetry, since the cell body and flagellar bundle are physically different units. The streamlines are closed as a consequence of the applied periodic boundary conditions, which implies differences in the far field compared to experimental observations. The effect of the boundary conditions is confirmed by the theoretical flow field for a finite-distance force dipole with the same boundary conditions in Fig. 7(b). The flow field for an infinite fluid domain is displayed in Fig. 3.

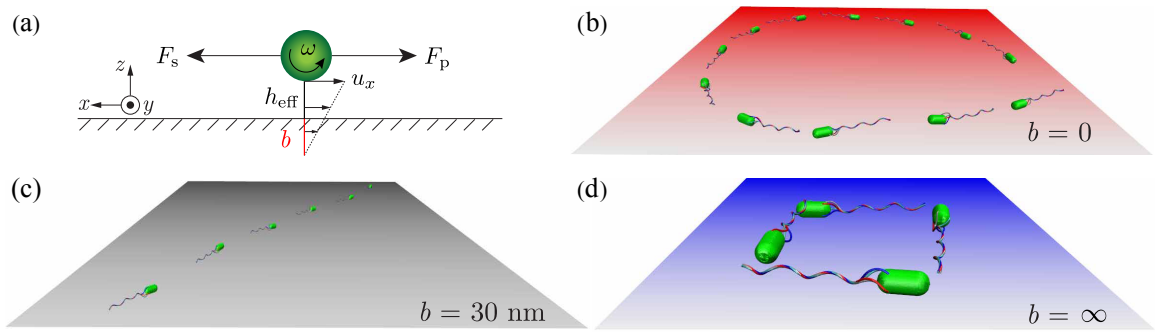

Fig. 8: *(a) The rotational motion with frequency ω of the bacterium body induces a shear flow for a surface with non-zero slip. The slip length b is the extrapolated distance inside the wall, where the shear velocity vanishes. (b) Clockwise, (c) noisy straight, and (d) counterclockwise trajectories of a bacterium swimming near homogeneous surfaces of slip lengths b. For details see Ref. [82].*

4.2 Swimming of *E. coli* at surfaces

Hydrodynamic interactions between swimmers and nearby walls determine their swimming behaviors [1, 50]. As shown in Fig. 8, different slip lengths—denoted by b—lead to different trajectories. For no-slip surfaces (glass, $b = 0$), a bacterium exhibits clockwise (CW) circular trajectories, whereas counterclockwise (CCW) circular trajectories are obtained for slip boundaries (air-water interface, $b = \infty$) [50, 80]. Typically, a surface exhibits partial slip due to adsorbents, microstructures, and hydrophobicity. A trajectory switches from CW to CCW (or vice versa) when b reaches some characteristic value (cf. Fig. 8(c)). Such a transition has been observed experimentally for *E. coli* swimming near glass surfaces upon addition of alginate, and has been attributed to changes in the slip length [81]. The simulation results presented in Ref. [82] show that swimming *E. coli* bacteria are able to sense surface slip on the nanoscale. This fact can be exploited to direct bacterial motion [82]. Further aspects on swimmer-surface interactions are presented in the lecture D.4 *Swimming near surfaces* by J. Elgeti and G. Gompper.

5 Conclusions

Hydrodynamics and hydrodynamic interactions are indispensable for biological microswimmers. The long-range nature of hydrodynamic interactions and hydrodynamic long-time tails combined with the autonomous microswimmer motion give rise to peculiar phenomena such as dipolar flow fields, synchronization of flagellar motion/beating, or collective phenomena [1]. Moreover, hydrodynamic interactions with surfaces govern the microswimmer dynamics adjacent to walls and cause particular trajectories. The latter provides a route to control the swimming behavior of bacteria such as *E. coli* [54].

Mesoscale hydrodynamic simulation approaches are extremely valuable tools to study soft matter systems. Specifically, the MPC approach developed into a versatile tool to study hydrodynamic properties of complex fluids since it has been introduced in 1999 [24]. By now, several collision algorithms have been proposed and employed, and the method has been generalized to describe multi-phase flows [83] and viscoelastic fluids [26, 84, 85]. A major advantage of the

algorithm is its easy coupling to the dynamics of embedded particles using a hybrid MPC-MD simulations approach. Results of such studies are in excellent quantitative agreement with both theoretical predictions and results obtained using other simulation techniques. In the future, we will see more applications of the method in non-equilibrium and driven soft-matter systems; specifically for systems where thermal fluctuations play a major role. Here, the full advantage of the method can be exploited, because the interactions of colloids, polymers, and membranes with the mesoscale fluid can be treated on the same basis.

References

[1] J. Elgeti, R. G. Winkler, and G. Gompper, Rep. Prog. Phys. **78**, 056601 (2015).

[2] J. M. Yeomans, D. O. Pushkin, and H. Shum, Eur. Phys. J. Spec. Top. **223**, 1771 (2014).

[3] E. Lauga and T. R. Powers, Rep. Prog. Phys. **72**, 096601 (2009).

[4] D. B. Kearns, Nat. Rev. Microbiol. **8**(9), 634 (2010).

[5] M. Polin, I. Tuval, K. Drescher, J. P. Gollub, and R. E. Goldstein, Science **325**(5939), 487 (2009).

[6] R. Stocker and W. M. Durham, Science **325**(5939), 400 (2009).

[7] B. Afzelius, Science **193**(4250), 317 (1976).

[8] Q. Wang, J. Pan, and W. J. Snell, Cell **125**, 549 (2006).

[9] J. H. E. Cartwright, O. Piro, and I. Tuval, Proc. Natl. Acad. Sci. USA **101**(19), 7234 (2004).

[10] E. M. Purcell, Am. J. Phys. **45**(1), 3 (1977).

[11] J. Sivinski, in *Sperm Competition and the Evolution of Animal Mating Systems*, edited by R. L. Smith (Academic, Orlando, 1984), p. 174.

[12] H. H. Wensink, J. Dunkel, S. Heidenreich, K. Drescher, R. E. Goldstein, H. Löwen, and J. M. Yeomans, Proc. Natl. Acad. Sci. USA **109**, 14308 (2012).

[13] N. C. Darnton, L. Turner, S. Rojevsky, and H. C. Berg, Biophys. J. **98**, 2082 (2010).

[14] M. A. Sleigh, *The Biology of Cilia and Flagella* (Pergamon Press, Oxford, 1962).

[15] P. J. Hoogerbrugge and J. M. V. A. Koelman, Europhys. Lett. **19**, 155 (1992).

[16] P. Español, Phys. Rev. E **52**, 1734 (1995).

[17] P. Español and P. B. Warren, Europhys. Lett. **30**, 191 (1995).

[18] G. R. McNamara and G. Zanetti, Phys. Rev. Lett. **61**, 2332 (1988).

[19] X. Shan and H. Chen, Phys. Rev. E **47**, 1815 (1993).

[20] X. He and L.-S. Luo, Phys. Rev. E **56**, 6811 (1997).

[21] G. A. Bird, *Molecular Gas Dynamics and the Direct Simulation of Gas Flows* (Oxford University Press, Oxford, 1994).

[22] F. J. Alexander and A. L. Garcia, Comp. in Phys. **11**, 588 (1997).

[23] A. L. Garcia, *Numerical Methods for Physics* (Prentice Hall, 2000).

[24] A. Malevanets and R. Kapral, J. Chem. Phys. **110**, 8605 (1999).

[25] R. Kapral, Adv. Chem. Phys. **140**, 89 (2008).

[26] G. Gompper, T. Ihle, D. M. Kroll, and R. G. Winkler, Adv. Polym. Sci. **221**, 1 (2009).

[27] L. D. Landau and E. M. Lifshitz, *Fluid Mechanics* (Pergamon Press, London, 1959).

[28] J. P. Boon and S. Yip, *Molecular Hydrodynamics* (Dover, New York, 1980).

[29] J.-P. Hansen and I. R. McDonald, *Theory of Simple Liquids* (Academic Press, London, 1986).

[30] H. Risken, *The Fokker-Planck Equation* (Springer, Berlin, 1989).

[31] J. K. G. Dhont, *An Introduction to Dynamics of Colloids* (Elsevier, Amsterdam, 1996).

[32] E. Lauga, Phys. Fluids **19**(6), 061703 (2007).

[33] M. Theers and R. G. Winkler, Soft Matter **10**, 5894 (2014).

[34] M. Doi and S. F. Edwards, *The Theory of Polymer Dynamics* (Clarendon Press, Oxford, 1986).

[35] E. Lauga, Soft Matter **7**, 3060 (2011).

[36] C.-C. Huang, G. Gompper, and R. G. Winkler, Phys. Rev. E **86**, 056711 (2012).

[37] B. J. Alder and T. E. Wainwright, Phys. Rev. A **1**, 18 (1970).

[38] R. Zwanzig and M. Bixon, Phys. Rev. A **2**, 2005 (1970).

[39] M. H. Ernst, E. H. Hauge, and J. M. J. van Leeuwen, Phys. Rev. A **4**, 2055 (1971).

[40] E. Hauge and A. Martin-Löf, Journal of Statistical Physics **7**, 259 (1973).

[41] E. J. Hinch, J. Fluid Mech. **72**, 499 (1975).

[42] G. L. Paul and P. N. Pusey, J. Phys. A **14**, 3301 (1981).

[43] B. U. Felderhof, J. Chem. Phys. **123**, 044902 (2005).

[44] C. C. Huang, G. Gompper, and R. G. Winkler, J. Chem. Phys. **138**, 144902 (2013).

[45] M. Theers and R. G. Winkler, Phys. Rev. E **88**, 023012 (2013).

[46] A. Pikovsky, M. Rosenblum, and J. Kurths, *Synchronization: A Universal Concept in Nonlinear Science* (Cambridge University Press, 2002).

[47] S. H. Strogatz, *Sync: How Order Emerges From Chaos In the Universe, Nature, and Daily Life* (Hyperion, 2004).

[48] P. Lenz and A. Ryskin, Phys. Biol. **3**, 285 (2006).

[49] R. G. Winkler, J. Chem. Phys. **127**, 054904 (2007).

[50] E. Lauga, W. R. DiLuzio, G. M. Whitesides, and H. A. Stone, Biophys. J. **90**, 400 (2006).

[51] B. Rodenborn, C.-H. Chen, H. L. Swinney, B. Liu, and H. P. Zhang, Proc. Natl. Acad. Sci. USA **110**(5), E338 (2013).

[52] T. Ishikawa, J. R. Soc. Interface **6**, 815 (2009).

[53] K. Drescher, J. Dunkel, L. H. Cisneros, S. Ganguly, and R. E. Goldstein, Proc. Natl. Acad. Sci. USA **10940**, 108 (2011).

[54] J. Hu, M. Yang, G. Gompper, and R. G. Winkler, Soft Matter (2015).

[55] E. Allahyarov and G. Gompper, Phys. Rev. E **66**, 036702 (2002).

[56] H. Noguchi, N. Kikuchi, and G. Gompper, EPL **78**, 10005 (2007).

[57] H. Noguchi and G. Gompper, Phys. Rev. E **78**, 016706 (2008).

[58] A. Malevanets and R. Kapral, J. Chem. Phys. **112**, 7260 (2000).

[59] R. G. Winkler, in *Hierarchical Methods for Dynamics in Complex Molecular Systems*, edited by J. Grotendorst, G. Sutmann, G. Gompper, and D. Marx (Forschungszentrum Jülich GmbH, Jülich, 2012), vol. 10 of *IAS Series*.

[60] C.-C. Huang, A. Chatterji, G. Sutmann, G. Gompper, and R. G. Winkler, J. Comput. Phys. **229**, 168 (2010).

[61] T. Ihle and D. M. Kroll, Phys. Rev. E **63**, 020201(R) (2001).

[62] T. Ihle and D. M. Kroll, Phys. Rev. E **67**, 066705 (2003).

[63] R. G. Winkler and C.-C. Huang, J. Chem. Phys. **130**, 074907 (2009).

[64] M. Ripoll, K. Mussawisade, R. G. Winkler, and G. Gompper, Phys. Rev. E **72**, 016701 (2005).

[65] C.-C. Huang, A. Varghese, G. Gompper, and R. G. Winkler, Phys. Rev. E **91**, 013310 (2015).

[66] A. Malevanets and J. M. Yeomans, Europhys. Lett. **52**, 231 (2000).

[67] M. Ripoll, K. Mussawisade, R. G. Winkler, and G. Gompper, Europhys. Lett. **68**, 106 (2004).

[68] K. Mussawisade, M. Ripoll, R. G. Winkler, and G. Gompper, J. Chem. Phys. **123**, 144905 (2005).

[69] S. Poblete, A. Wysocki, G. Gompper, and R. G. Winkler, Phys. Rev. E **90**, 033314 (2014).

[70] M. P. Allen and D. J. Tildesley, *Computer Simulation of Liquids* (Clarendon Press, Oxford, 1987).

[71] W. C. Swope, H. C. Andersen, P. H. Berens, and K. R. Wilson, J. Chem. Phys. **76**, 637 (1982).

[72] S. H. Lee and R. Kapral, J. Chem. Phys. **121**, 11163 (2004).

[73] A. Lamura, G. Gompper, T. Ihle, and D. M. Kroll, Europhys. Lett. **56**, 319 (2001).

[74] Y. Inoue, Y. Chen, and H. Ohashi, J. Stat. Phys. **107**, 85 (2002).

[75] I. O. Götze, H. Noguchi, and G. Gompper, Phys. Rev. E **76**, 046705 (2007).

[76] J. K. Whitmer and E. Luijten, J. Phys.: Condens. Matter **22**, 104106 (2010).

[77] M. Yang and M. Ripoll, Soft Matter **10**, 1006 (2014).

[78] H. Yamakawa, *Helical Wormlike Chains in Polymer Solutions* (Springer-Verlag, Berlin Heidelberg, 1997).

[79] R. Vogel and H. Stark, Eur. Phys. J. E **33**, 259 (2010).

[80] R. Di Leonardo, D. Dell'Arciprete, L. Angelani, and V. Iebba, Phys. Rev. Lett. **106**, 038101 (2011).

[81] L. Lemelle, J.-F. Palierne, E. Chatre, C. Vaillant, and C. Place, Soft Matter **9**, 9759 (2013).

[82] J. Hu, A. Wysocki, R. G. Winkler, and G. Gompper, Sci. Rep. **5**, 9586 (2015).

[83] E. Tüzel, G. Pan, T. Ihle, and D. M. Kroll, EPL **80**, 40010 (2007).

[84] Y.-G. Tao, I. O. Götze, and G. Gompper, J. Chem. Phys. **128**, 144902 (2008).

[85] B. Kowalik and R. G. Winkler, J. Chem. Phys. **138**, 104903 (2013).